Journal of Power Sources 418 (2019) 61–73

Contents lists available at ScienceDirect

Journal of Power Sources

journal homepage: www.elsevier.com/locate/jpowsour

Electrochemical-thermal modeling of lithium plating/stripping of Li($Ni_{0.6}Mn_{0.2}Co_{0.2}$)O_2/Carbon lithium-ion batteries at subzero ambient temperatures

Xinchen Zhao, Yilin Yin, Yang Hu, Song-Yul Choe*

Department of Mechanical Engineering, Auburn University, AL, 36849, USA

HIGHLIGHTS

- Degradation caused by lithium plating/stripping is electrochemically modeled.
- Lithium plating is analyzed based on the charge and mass transfer limitations.
- Differential voltage analysis is used to calculate the amount of reversed capacity.
- The electrochemical model is validated for both BoL and EoL.

GRAPHICAL ABSTRACT

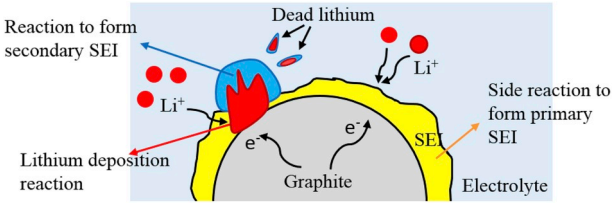

ARTICLE INFO

Keywords:
Degradation
Lithium plating
Lithium stripping
Subzero temperature

ABSTRACT

Electrochemical performance of lithium-ion batteries drops significantly at low temperatures, especially under charging, because the lithium ions are prone to deposit as lithium metal on instead of intercalating into the solid matrix of anode. At discharging, the existence of lithium stripping leads to the capacity reversed partially, whose amount is proportional to the width of extra voltage plateau displayed at the beginning. A physics-based electrochemical-thermal model considering effects of lithium plating/stripping is developed and validated to explore the degradation mechanism and behaviors of NMC/Carbon cells undergoing prolonged cycling. The temporal and spatial analyses of overpotential of lithium plating and surface concentration in solid phase at various operating conditions demonstrate that lithium plating starts to take place at the interface between composite anode and separator, and the degradation can be accelerated by the decreasing ambient temperatures and increasing charging current rates. The degradation effects including loss of recyclable lithium ions, loss of anode active material, growth of plated lithium and secondary solid electrolyte interphase (SEI) and consumption of electrolyte solvents are considered. The model is capable of estimating capacity as a function of cycle number with an overall accuracy of 3% if the capacity fade is less than 30%.

1. Introduction

Lithium ion batteries (LiBs), usually having carbon as anode, are widely used for portable devices, such as laptops and mobile phones, and electric vehicles (EVs), for the characteristics of high power and energy density and long lifespan. When LiBs are operated in low ambient temperatures, the capability of delivering or accepting energy or power drops, which is a dramatic limitation of lifetime and safety issues. Particularly under charging, the lithium ions are inclined to form metallic lithium that is deposited on instead of intercalating into the negative electrode, which is called “lithium plating”, also known as “lithium deposition reaction”. As unwanted side reaction, the lithium

* Corresponding author. 1418 Wiggins Hall, Auburn University, AL, 36849, USA.
E-mail address: choeson@auburn.edu (S.-Y. Choe).

https://doi.org/10.1016/j.jpowsour.2019.02.001
Received 2 November 2018; Received in revised form 15 January 2019; Accepted 1 February 2019
Available online 15 February 2019
0378-7753/ © 2019 Elsevier B.V. All rights reserved.

Nomenclature

A	sandwich area of the cell (m^2)
a_s	specific surface area of electrode (m^{-1})
c	ion concentration (mol L^{-1})
D	diffusion coefficient(m^2 s^{-1})
F	Faraday constant (96,487C mol^{-1})
I	current of the cell (A)
i_0	exchange current density of intercalation (Am^{-2})
j^{Li}	reaction rate of intercalation (Am^{-3})
k_s	isolation coefficient due to SEI
L	thickness of the micro cell (cm)
Q	capacity of the cell (Ah)
q	amount of ion loss caused by side reaction (Ah)
R	resistance (Ω m^2) or universal gas constant (8.314 J mol^{-1} K^{-1})
R_s	radius of spherical electrode particle (m)
r	coordinate along the radius of electrode particle (m)
T	cell temperature (K)
t	time (s)
U	potential (V)
V	voltage (V) or volume of the composite electrode (m^3)
$\tilde{V}$	molar volume (m^3 mol^{-1})
x	stoichiometric number of the anode
y	stoichiometric number of the cathode

Greek symbols

A	transfer coefficient for an electrode reaction
Δ	thickness (m)
E	volume fraction of a porous medium
ϕ	potential (V)
η	over-potential of electrode reaction (V)
κ	ionic conductivity (S m^{-1})
σ	conductivity (S m^{-1})

Subscripts and Superscripts

a	anodic
ave	average value
c	cathodic
e	electrolyte phase
eff	effective
eq	equilibrium
error	error
exp	experiment
Li	*lithium* ion
main	main reaction
max	maximum
r	radial direction in electrode particle
s	solid phase
p	Lithium plating
sim	simulation
surf	electrode particle surface
0%	0% SoC
100%	100% SoC
+	positive electrode (cathode)
-	negative electrode (anode)

deposition reaction leads to capacity and power fade, impedance rise, and the growth of dendritically metallic lithium even triggers internal short circuit [1]. Therefore, understanding of mechanisms and effects of the lithium deposition reaction on battery performances at low temperatures is of crucial significance for safe and durable design of LiB systems.

At the temperatures larger than 0 °C, side reaction is regarded as the predominant cause for degradation and is accelerated by the elevated temperatures, large SoC cycling limits and high SoC levels, which has been extensively investigated [2–7]. Lithium ions and electrolyte solvents take part in side reaction at the interface between electrode and electrolyte to form the unsolvable byproducts, lithium carbonate (Li_2CO_3) and lithium ethylene dicarbonate ($(CH_2OCO_2Li)_2$), which are the main compounds in solid electrolyte interphase (SEI). In contrast, at low temperatures, due to the sluggish charge transfer kinetics and low diffusivities of lithium ions, lithium deposition reaction is prone to take place. Schematic diagram of degradation mechanisms on anode at low temperatures is depicted in Fig. 1. At initial cycles, a thin layer (primary SEI: Yellow Color) is formed at the interface between carbon particles and electrolyte to protect the electrode from further corrosion and the electrolyte from being decomposed by participating in chemical side reaction. Since the SEI is conductive to lithium ions, but isolative to electrons, lithium plating occurs at the interface between carbon particles and the primary SEI to form metallic lithium (Red Color) at low temperatures. The plated lithium can react with electrolyte solvents to form the secondary SEI (Blue Color) that has the same compounds as the primary SEI. Formation of the primary SEI, plated lithium, and secondary SEI only occur under charging.

At discharging, the plated lithium can be partially dissolved and extra lithium ions are released, which results in a certain amount of reversible capacity, called “lithium stripping”, also known as “lithium dissolution reaction”. If the dissolved lithium ions are unfortunately fully covered by the SEI, the ions are isolated, which is called “dead lithium”, resulting in the irreversible capacity loss. Therefore, the lithium deposition/dissolution reaction contains both reversible and irreversible processes that are accelerated by the decreasing temperatures.

Due to the detrimental effects of lithium plating on battery performances, considerable efforts have been made to develop methods to detect the onset of metallic lithium and its growth, experimentally and mathematically. In-situ and ex-situ experimental techniques have been proposed [8]. The in-situ experiments [9–12] include constant charging/discharging, incremental capacity measurement, differential analysis [13] and electrochemical impedance spectroscopy (EIS) etc. in the field of electrochemistry, while in-situ neutron diffraction method [14,15] in the field of material. The ex-situ techniques mainly imply to the postmortem analysis [16], such as SEM [17–21], XRD [22,23], XPS [24], and TEM [25]. Liao et al. [26] investigated the structural change of the lithiation and delithiation using first-principle techniques. However, in most cases, only the dendrite-like morphology has been detected without any evidence of the compounds in the deposits. Moreover, few calculate the amount of the plated lithium quantitatively.

Numerical approach by modeling the behaviors of lithium plating is a great way to quantify the amount of plated lithium. Arora et al. [27] firstly proposed the equations that describe the lithium deposition reaction at overcharge based on Doyle's model [28]. Tang et al. [29] improved the Arora's model to 2D and found that the lithium deposition

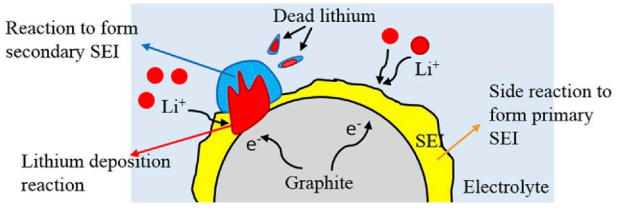

Fig. 1. Schematic diagram of degradation mechanisms at low temperature.

Table 1
Specifications of testing cells.

Material	Cathode	NMC622 ($Li(Ni_{0.6}Mn_{0.2}Co_{0.2})O_2$)
	Anode	Carbon
End-of-charge (EoC) voltage, current		4.2V, 3A
End-of-discharge (EoD) voltage		2.5V
Nominal capacity @ 1/3C-rate		58.9Ah
Dimension (mm^3)		99.7 × 301.5 × 13.3

tended to occur at electrode edges and an extension of the anode edge was capable of preventing the onset of lithium plating. Perkins et al. [30] developed a control-oriented reduced order model (ROM) of lithium overcharge deposition in order to accomplish an optimal design of a tradeoff between LiB performance and durability. Most recently, Ge et al. [31] validated the charging behaviors of fresh cells at low temperatures and extracted part of parameters by nuclear magnetic resonance (NMR). Yang et al. [32] proposed a physics-based aging model considering lithium plating to describe the transition from linear to nonlinear behaviors at room temperature. However, none of the electrochemical model was capable of estimating the degradation effects caused by both lithium plating and lithium stripping simultaneously at low temperatures.

In this paper, effects of lithium plating and lithium stripping on the degradation will be experimentally analyzed and quantified, which enables to predict the capacity and power fade, particularly at subzero temperatures. The degradation effects during prolonged cycles are firstly quantified, including loss of recyclable lithium ions, loss of active material (AM), growth of plated lithium and secondary SEI, and the consumption of electrolyte. In addition, a physics-based electrochemical-thermal model considering lithium plating/stripping is developed and firstly validated against both fresh and aged cells at different operating conditions, including temperatures, charging and discharging C-rates. The experimental analysis at subzero temperatures, including test matrices and the evidence of existence of lithium plating, are summarized in section 2. The principles and equations of the electrochemical-thermal model are discussed in section 3. The model validations and analyses of different electrochemical parameters are presented in section 4. The conclusion is section 5.

2. Experiment

The experimental LiBs investigated in this paper are pouch-type NMC/Carbon ones, whose specifications are summarized in Table 1. A programmable power supply and electric-load are connected in parallel to supply the programmed charging and discharging current profiles. The impedance spectra are measured by EIS equipment, GAMRY, and the parameters are extracted by fitting the equivalent circuit model (ECM).

To explore the performance of fresh cells at low temperatures, the open-circuit voltage (OCV) as a function of state-of-charge (SoC) is measured at the ambient temperature of −20 °C by a very small current of 1/30 C-rate (≈2A) with sufficient resting time no less than 1h at each testing point in order to allow the terminal voltage and OCV to be equal in the maximum likelihood. For beginning-of-life (BoL), the cell is charged by a constant current (CC) followed by a constant voltage (CV, 4.2V) protocol until reaching a cutoff current of 3A. After resting for 30 min, the cell continues to be discharged by CC to 2.5V. The constant current applied at charging and discharging profile varies among 1/2C-rate, 1/3C-rate, 1/4C-rate and 1/10C-rate at different temperatures (−20/-25/-30 °C).

For end-of-life (EoL), the cells are involved into the cycling tests according to the test matrix summarized in Table 2. Effects of operating temperatures (0/-10/-20/-25/-30 °C), charging and discharging current rates (1/3C-rate, 1/4C-rate) on the electrochemical performance of LiBs are discussed. Each consecutive cycle is performed by a CC−CV

Table 2
Test matrix.

Effects of temperatures

Temp. (°C)	Charge/discharge current	SoC cycling limit	Cycle No.	Capacity fade
0	0.25C/0.25C	0–100%	8	1.4%
−10			8	1.7%
−20			8	24.1%
−25			6	21.1%
−30			6	43.9%

Effects of charging/discharging C-rate

Temp. (°C)	Charge/discharge current	SoC cycling limit	Cycle No.	Capacity fade
−20	(1/3)C/(1/3)C	0–100%	8	29.8%
	0.25C/(1/3)C			14.3%
	0.25C/0.25C			24.1%

charging and CC discharging protocol. Periodically, the cell is detached from cycling and conduct a series of reference performance tests (RPTs) at 25 °C, including the measurements of capacity and EIS. In each RPT, the capacity is measured as follows: (1) Charge the cell using a CC−CV protocol (CC: 1/3C-rate, CV: 4.2V, EoC current: 3A); (2) Rest for 30 min; (3) Discharge the cell by 1/3C-rate current to 2.5V. EIS is measured: (1) Charge the cell to 50% SoC by 1/3C-rate CC; (2) Rest for 3h; (3) Conduct EIS test at the frequency from 10 mHz to 1 kHz. After cycling, the cells are discharged to 0% SoC and dissembled in a glove box fulfilled with argon gas to perform post-mortem analysis. The morphological variation and identification of the compounds in the deposits are performed by SEM and FTIR, respectively.

Fig. 2 (a) presents the capacity retention of the cells cycled at different operating conditions. The upper subplot shows the capacity retention at various temperatures (−30–0 °C). In order to allow the lithium plating/stripping to take place to the most degree, the cells cycled at the temperatures lower than −20 °C become preferential selections. The lower subplot shows the capacity retention at various charging and discharging current rates (1/3C-rate, 1/4C-rate). When the cell is charged at the same current, the same amount of lithium metal is plated. Due to the existence of lithium stripping at discharge, larger discharging C-rates promote the exfoliation of plated lithium, resulting in more capacity reversed and less capacity fade. When the same discharging current is applied, larger charging current leads to more lithium plating formed and more capacity fade.

EIS spectra of the cells cycled by 1/4C-rate current at the temperatures of −20 °C, −25 °C and −30 °C are shown in Fig. 2 (b), (c) and (d), respectively. The impedance spectra shift rightwards as the augment of cycle number, which denotes the increase of Ohmic resistance, including the resistance of electrode, electrolyte and current collectors. SEI resistance represented by the radius of the semi-circle in the Nyquist plot varies a little in the first several cycles but increases much in the last two cycles. The detailed analysis of the relationship between capacity retention and the extracted Ohmic and SEI resistances by the ECM of the cell cycled at the same operating condition as Fig. 2 (b) is plotted in Fig. 2 (e). The slight variation of SEI resistance at the first 6 cycles implies that the ignorance of side reaction at temperatures below −20 °C is reasonable, while the increase of SEI resistance at the last 2 cycles result from the secondary SEI formation. Fig. 2 (f) shows the FTIR analyses of the cells cycled at various operating conditions. The peak around 1400 cm^{-1} paired with a peak around 860 cm^{-1} represent the vibration of CO_3^- anions and $ROCO_2$ containing species. For EC based electrolyte, it manifests the existence of the compounds, Li_2CO_3 and $ROCO_2Li$, which are the main components of SEI. Due to the ignorance of side reaction, the SEI detected by FTIR comes from the products of the reaction between lithium metal and electrolyte solvents,

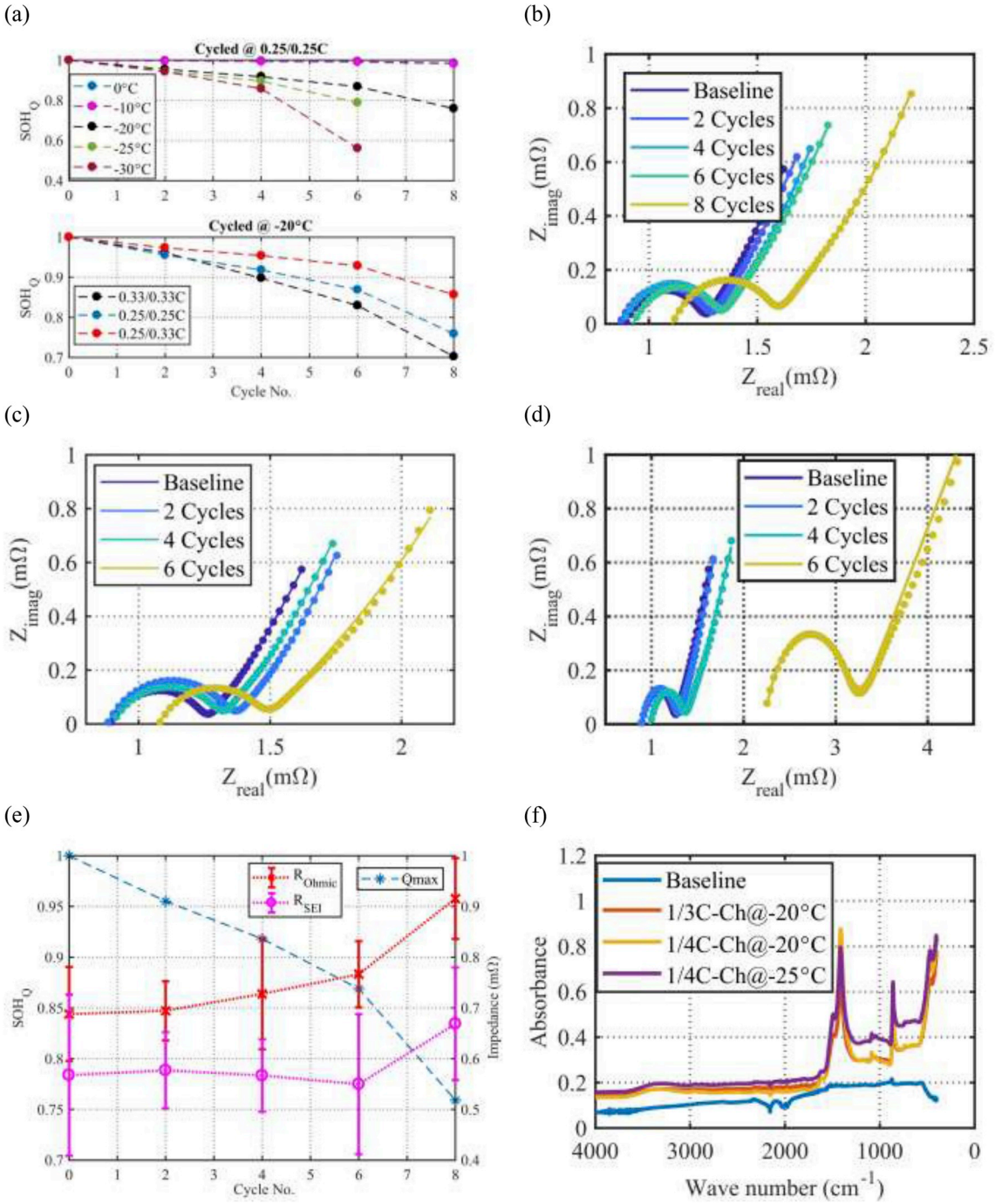

Fig. 2. Experimental analyses. (a) Capacity retention at different cycling conditions, including operating temperatures, charging and discharging current rates; (b) Impedance spectra of the cell cycled by1/4C-rate charging/discharging current at −20 °C; (c) Impedance spectra of the cell cycled by1/4C-rate charging/discharging current at −25 °C; (d) Impedance spectra of the cell cycled by1/4C-rate charging/discharging current at −30 °C; (e) Capacity retention, Ohmic and SEI resistance extracted from the cell cycled by 1/4C-rate charging/discharging current at −20 °C; (f) FTIR analyses of cells cycled at various operating conditions.

which can be regarded as an indirect evidence of the existence of lithium plating.

3. Model description

A well-established reduced order model (ROM) [33,34] has been developed in our previous study to describe the electrochemical behaviors of LiBs, including intercalation/de-intercalation of lithium ions to/from the electrode, kinetics of electrochemical reaction taking place at the interface between electrode and electrolyte, ion transportation and diffusion through electrode and electrolyte, whose governing equations and their corresponding boundary conditions are summarized in Table 3. Detailed explanations can be found in the references. Only modifications made to incorporate the lithium deposition/dissolution reaction at low temperatures are described in the following sections.

In order to develop a physics-based electrochemical model to investigate the electrochemical performances of both fresh and aged LiBs at low temperatures, some assumptions need to be made in advance.

- Degradation only takes place on anode.
- Lithium deposition reaction is semi-reversible, which implies that

Table 3
Governing equations of the FOM and ROM.

	FOM	Reduction method	ROM	
Ion concentration in electrode	$\frac{\partial c_s}{\partial t} = \frac{D_s}{r^2}\frac{\partial}{\partial r}\left(r^2\frac{\partial c_s}{\partial r}\right)$; $\left.\frac{\partial c_s}{\partial r}\right\|_{r=0_1} = 0$; $D_s\left.\frac{\partial c_s}{\partial r}\right\|_{r=R_s} = \frac{-j^{Li}}{a_s F}$	Polynomial approach	$\frac{d}{dt}c_{s,ave} + 3\frac{j^{Li}}{R_s a_s F} = 0$ $\frac{d}{dt}q_{ave} + 30\frac{D_s}{R_s^2}q_{ave} + \frac{45}{2}\frac{j^{Li}}{R_s^2 a_s F} = 0$ $35\frac{D_s}{R_s}(c_{s,surf} - c_{s,ave}) - 8D_s q_{ave} = \frac{-j^{Li}}{a_s F}$	(1)
Ion concentration in electrolyte	$\frac{\partial(\varepsilon_e c_e)}{\partial t} = \frac{\partial}{\partial x}\left(D_e^{\text{eff}}\frac{\partial}{\partial x}c_e\right) + \frac{1-t_+^0}{F}j^{\text{Li}}$ $\left.\frac{\partial c_e}{\partial t}\right\|_{x=0} \frac{\partial c_e}{\partial t}\Big\|_{x=L} = 0$	State space approach	$\dot{\mathbf{c}}_\mathbf{e} = \mathbf{A}\cdot\mathbf{c}_\mathbf{e} + \mathbf{B}\cdot I$ $\mathrm{y} = \mathbf{C}\cdot\mathbf{c}_\mathbf{e} + \mathbf{D}\cdot I$	(2)
Ohm's law in electrode	$\frac{\partial}{\partial x}\left(\sigma^{\text{eff}}\frac{\partial}{\partial x}\varphi_s\right) - j^{\text{Li}} = 0$ $-\sigma^{\text{eff}}\frac{\partial}{\partial x}\varphi_s\Big\|_{x=0} = -\sigma^{\text{eff}}\frac{\partial}{\partial x}\varphi_s\Big\|_{x=L} = \frac{I}{A}$ $\frac{\partial}{\partial x}\varphi_s\Big\|_{x=L_-} = \frac{\partial}{\partial x}\varphi_s\Big\|_{x=L_-+L_{\text{sep}}} = 0$		$\frac{\partial}{\partial x}\left(\sigma^{\text{eff}}\frac{\partial}{\partial x}\varphi_s\right) - j^{\text{Li}} = 0$ $-\sigma^{\text{eff}}\frac{\partial}{\partial x}\varphi_s\Big\|_{x=0} = -\sigma^{\text{eff}}\frac{\partial}{\partial x}\varphi_s\Big\|_{x=L} = \frac{I}{A}$ $\frac{\partial}{\partial x}\varphi_s\Big\|_{x=L_-} = \frac{\partial}{\partial x}\varphi_s\Big\|_{x=L_-+L_{\text{sep}}} = 0$	(3)
Ohm's law in electrolyte	$\frac{\partial}{\partial x}\left(\kappa^{\text{eff}}\frac{\partial}{\partial x}\varphi_e\right) + \frac{\partial}{\partial x}\left(\kappa_D^{eff}\frac{\partial}{\partial x}\ln c_e\right) + j^{\text{Li}} = 0$ $\frac{\partial}{\partial x}\varphi_e\Big\|_{x=0} = \frac{\partial}{\partial x}\varphi_e\Big\|_{x=L} = 0$	Simplification	$\frac{\partial}{\partial x}\left(\kappa^{\text{eff}}\frac{\partial}{\partial x}\varphi_e\right) + j^{\text{Li}} = 0$	(4)
Electrochemical kinetics	$j^{\text{Li}} = a_s i_0\left\{\exp\left[\frac{\alpha_a F}{RT}\eta\right] - \exp\left[-\frac{\alpha_c F}{RT}\eta\right]\right\}$ $\eta = \varphi_s - \varphi_e - U_{eq}$	Linearization	$j^{Li} = \frac{a_s i_0 F}{RT}\eta$	(5)

the reduction rate is 2 times of the oxidation rate.

- Film at the surface of anode particles in aged cells is a mixture of plated lithium, primary and secondary SEI.
- Both the primary and secondary SEI are only a mixture of Li_2CO_3 and $(CH_2OCO_2Li)_2$.
- Primary SEI formed at initial cycles is considered as constant.
- No mechanical failure nor gas generation is considered.
- No overcharge or undercharge process is considered.

In the present model, the lithium deposition reaction is considered as side reaction, which competes with intercalation on anode at low temperatures. If the local anode overpotential becomes negative referring to Li^+/Li ($\eta_{Li^+/Li} < 0$), due to the charge transfer limitation, lithium ions are inclined to deposit on instead of intercalating into the negative electrode, as described in Eq. (6).

$$Li^+ + e^- \leftrightarrow Li\ (s) \tag{6}$$

The total reaction rate (j_{total}^{Li}), can be divided to two components, main reaction rate (j^{Li}), and lithium deposition reaction rate ($j_{plating}^{Li}$). Both of main and lithium deposition reaction rate can be described using Butler-Volmer (BV) equation, as presented in Eq. (5) and Eq. (8), respectively. The lithium deposition reaction rate is selected from the minimum between 0 and $j_{plating}^{Li}$.

$$j_{total}^{Li} = j^{Li} + j_{plating}^{Li} \tag{7}$$

$$j_{plating}^{Li} = a_s i_{0,p}\left\{\exp\left[\frac{\alpha_{a,p} n_p F}{RT}\eta_p\right] - \exp\left[-\frac{\alpha_{c,p} n_p F}{RT}\eta_p\right]\right\} \tag{8}$$

where $i_{0,p}$ is the exchange current density of lithium deposition reaction, which is a fitting parameter as a function of temperature due to the lack of reliable experimental data. n_p is the number of lithium ions involved in Eq. (6) with a value of 1. $\alpha_{a,p}$ and $\alpha_{c,p}$ are the dimensionless anodic and cathodic charge transfer coefficient, which are assumed to be a value of 0.33 and 0.67 [27], respectively, due to the assumption of semi-reversible lithium deposition reaction. The activation overpotential of lithium deposition reaction, η_p, is calculated by

$$\eta_p = \varphi_s - \varphi_e - U_{eq,p} - \frac{R_{film}}{a_s} j_{total}^{Li} \tag{9}$$

, where φ_s, φ_e are the electrode and electrolyte potential, respectively. $U_{eq,p}$, the equilibrium potential, equals to 0, because the measurement is compared with a reference of lithium metal. R_{film} is the overall resistance of the surface film, as defined in Eq. (10).

$$R_{film} = \varepsilon_{Li}\left(\frac{\delta_{film}}{\kappa_{Li}}\right) + \varepsilon_{Li_2CO_3}\left(\frac{\delta_{film}}{\kappa_{Li_2CO_3}}\right) + \varepsilon_{(CH_2OCO_2Li)_2}\left(\frac{\delta_{film}}{\kappa_{(CH_2OCO_2Li)_2}}\right) \tag{10}$$

where κ_{Li} is the electronic conductivity of the plated lithium.$\kappa_{Li_2CO_3}$ and $\kappa_{(CH_2OCO_2Li)_2}$ are the ionic conductivity of Li_2CO_3 and $(CH_2OCO_2Li)_2$, respectively. ε_{Li}, $\varepsilon_{Li_2CO_3}$, and $\varepsilon_{(CH_2OCO_2Li)_2}$ are the volume fraction of lithium metal, Li_2CO_3 and $(CH_2OCO_2Li)_2$ in the film, respectively. δ_{film} is the thickness of the coated surface film.

$$\delta_{film} = \delta_{SEI} + \delta_p \tag{11}$$

where δ_{SEI} and δ_p are the thickness of SEI and plated lithium, respectively.

3.1. Analysis of degradation effects

Since the lithium deposition reaction is partially irreversible, the lithium ions, as the reactants, are continuously consumed as shown in Eq. (6). q_{total}^{Li} is defined as the total amount of ion losses due to lithium deposition reaction, which can be calculated by integrating the reaction rate over the total volume of composite anode

$$q_{total}^{Li} = \int_{x=0}^{\delta_-}\left(\int_{t=0}^{t} j_p^{Li}(x,\tau)d\tau\right)Adx \tag{12}$$

where δ- is defined as the thickness of composite anode.

Since part of metallic lithium in contact with electrolyte can be oxidized to form secondary SEI, a dimensionless parameter, λ, is introduced to denote the fraction of plated lithium that forms secondary SEI. The material balance of SEI and plated lithium can be expressed as

$$\frac{\partial c_{SEI}}{\partial t} = -\frac{1}{2F}\lambda j_p^{Li} \tag{13}$$

$$\frac{\partial c_{Li}}{\partial t} = -\frac{1}{F}(1-\lambda) j_p^{Li} \tag{14}$$

where c_{SEI} and c_{Li} are the molar concentration of SEI and plated lithium per unit volume of anode. In the model, the graphite particles are assumed to be spherical, and the surface film is assumed to be uniform in

the thickness direction. As such, the amount of SEI and plated lithium can be transformed to an equivalent thickness of the surface film, defined as the ratio of the total volume of SEI and lithium metal to the specific surface area,

$$\frac{\partial \delta_{film}}{\partial t} = -\frac{\tilde{V}_{SEI}}{2a_s F} c_{SEI} - \frac{\tilde{V}_{Li}}{a_s F} c_{Li} \tag{15}$$

where $\tilde{V}_{SEI}$ and $\tilde{V}_{Li}$ are the molar volume of SEI and metallic lithium. The first and second term in the right side of Eq. (15) denotes the thickness change of SEI and plated lithium, respectively.

Since both primary and secondary SEI are isolative to electrons, the growth of SEI can limit the accessible area of composite anode, which causes the reduction of volume fraction of the active anode material, ε_s, leading to capacity fade, as shown in Eq. (16).

$$\Delta\varepsilon_s = -k_s a_s \delta_{film} \tag{16}$$

where k_s is a dimensionless coefficient.

Since the plated lithium can react with the contact electrolyte solvents to form the secondary SEI as shown in Eq. (17) and Eq. (18), the consumption of electrolyte solvents resulting in the power fade can be analyzed by the decrease of the volume fraction of electrolyte, ε_e, in Eq. (19).

$$2Li + EC \rightarrow CH_2 = CH_2 \uparrow + Li_2CO_3 \downarrow \tag{17}$$

$$2Li + 2EC \rightarrow CH_2 = CH_2 \uparrow + (CH_2OCO_2Li)_2 \downarrow \tag{18}$$

$$\frac{\partial \varepsilon_e}{\partial t} = -\frac{\alpha \tilde{V}_e}{\delta\_F} q_{total}^{Li} \tag{19}$$

where $\tilde{V}_e$ is the molar volume of the electrolyte. α is a dimensionless coefficient indicating how many moles of the electrolyte solvents are involved in the reaction when 1 mol of the lithium metal is consumed. Under the assumption of the same reaction rate of Eq. (17) and Eq. (18), α equals to 0.75. Correspondingly, the decrease of the volume fraction of the electrolyte solvents leads to a decrease of the effective diffusion coefficient in the electrolyte.

$$D_e^{eff} = D_e \cdot \varepsilon_e \tag{20}$$

4. Results and discussions

Some of geometric and morphologic parameters of the cells, such as thickness and particle radius etc., are provided by the manufacturer, while the others, such as stoichiometric number and diffusion coefficients of solid and electrolyte phase etc., are used from literature and then optimized based on the validated results. The list of the parameters can be found in Table 4. The temperature-dependent parameters, such as diffusion coefficients and exchange current density of lithium deposition reaction, are optimized by the means of the Arrhenius equation.

4.1. Analysis of lithium plating under charging

According to the literature review, the lithium plating criteria is discussed from two aspects, potential and concentration, which are related to charge and mass transfer processes, respectively. At low temperatures, the sluggish charge transfer kinetics introduces a large overpotential as soon as the current is applied, especially for a high current-rate whatever the initial SoC is, which is regarded as charge transfer limitation (CTL). If the cell is charged at a relatively low current-rate, the charge transfer is not a sufficient rate-limiting factor. The poor solid diffusivity of lithium ions can cause a large concentration gradient over the radial direction of the particles, resulting in the accumulation of lithium ions on the surface of carbon particles, which is called “mass transfer limitation” (MTL).

4.1.1. Charge transfer limitation (CTL)

When the temperatures are lower than −20 °C, lithium plating becomes the dominant cause for degradation of LiBs. The effects of temperatures and charging C-rates on the lithium plating are discussed in Fig. 3. Subplot (a) shows the comparison of terminal voltage under CC−CV charging between experiments and simulations at various temperatures (−20/-25/-30 °C). The solid lines and markers represent the experiments and simulations, respectively. The error of terminal voltage estimation is within 4%, which verifies the model accuracy, as shown in subplot (b).

The electrochemical kinetics of lithium plating are governed by the

Table 4
List of model parameters (a: Manufacture; b: model validation; c: literature).

Category	Parameter	Negative electrode	Separator	Positive electrode	unit	
Geometry and volume fractions	Thickness, δ	84×10^{-6}	8.9×10^{-6}	77.5×10^{-6}	m	a
	Particle radius, R_s	10.7×10^{-6}		17.5×10^{-6}	m	a
Li^+ concentrations	Stoichiometry at 0% SoC	0.3		0.81		b
	Stoichiometry at 100% SoC	0.77		0.49		b
	Average electrolyte concentration, c_e	1.2×10^3	1.2×10^3	1.2×10^3	mol m^{-3}	a
Kinetic and transport properties	Exchange current density coefficient, i_0	13.2×10^4		6.79×10^4	A m^{-2}	c
	Charge-transfer coefficient, α_a, α_c	0.5, 0.5		0.5, 0.5		c
	Solid phase diffusion coefficient, D_s	Ds = f(T)			m^2 s^{-1}	b
	Solid phase conductivity, σ	100		10	S m^{-1}	c
	Electrolyte phase Li^+ diffusion coefficient, D_e	De = f(T)			m^2 s^{-1}	b
	Bruggeman's porosity exponent, p	1.5	1.5	1.5		c
	Electrolyte phase ionic conductivity, κ	$\kappa = 1106 c_e \exp(-8900 c_e^{1.4})$			S m^{-1}	c
	Li^+ transference number, t_0^+	0.363	0.363	0.363		c
	Equilibrium potential of anode	$U_{eq-}(y)$ $= 8.00229 + 5.0647x - 12.578x^{0.5} - 8.6322 \times 10^{-4}x^{-1} + 2.1765 \times 10^{-5}x^{1.5} - 0.46016 \exp(15 \times (0.06 - x)) - 0.55364 \exp(-2.4326 \times (x - 0.92))$				c
Lithium deposition reaction model	Exchange current density of lithium deposition reaction, $i_{0,p}$	4.55×10^{-8} at −20 °C 5.0×10^{-8} at −25 °C 8.51×10^{-8} at −30 °C			A m^{-2}	b
	Standard equilibrium potential of lithium plating, $U_{eq,p}$	0			V	c
	Molar volume of Li, $\tilde{V}_{Li}$	7.69×10^4			mol m^{-3}	c
	isolation rate of active anode materials due to lithium plating, k_s	10				b
	molar volume of electrolyte, $\tilde{V}_e$	3.25×10^8			mol m^{-3}	c

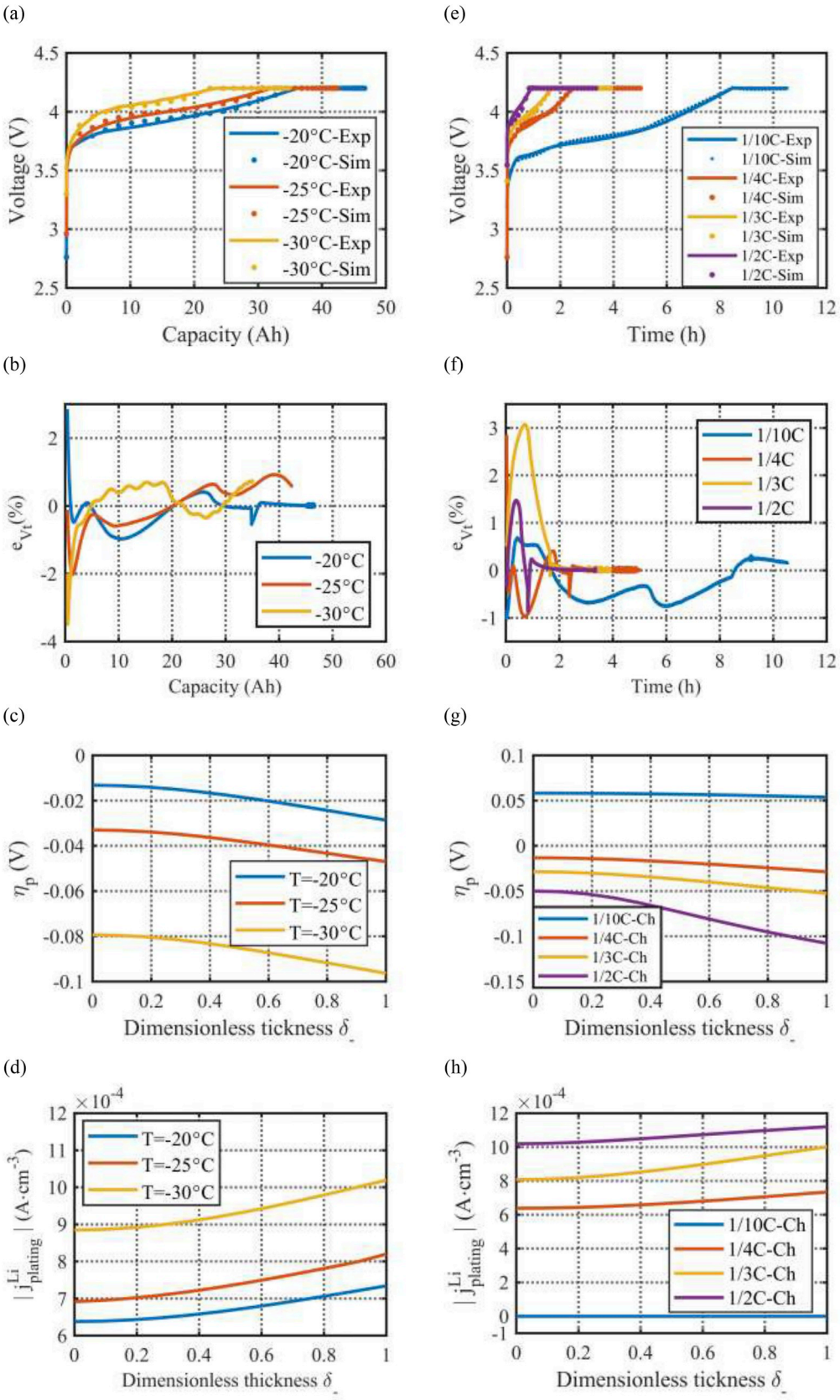

Fig. 3. Analysis of charging behaviors. (a) Comparison of charge behaviors between experimental data and simulation results at −20/-25 °C/-30 °C; (b) Error of terminal voltage estimation at −20/-25 °C/-30 °C; (c) Distribution of overpotential of lithium plating at −20/-25/30 °C; (d) Distribution of lithium deposition reaction rate at −20/-25/30 °C; (e) Comparison of charge behaviors between experimental data and simulation results at different charging C-rates (1/10C, 1/4C, 1/3C and 1/2C, respectively) at −20 °C; (f) Error of terminal voltage estimation when charged at 1/10C, 1/4C, 1/3C and 1/2C, respectively; (g) Distribution of overpotential of lithium plating when charged at 1/10C, 1/4C, 1/3C and 1/2C, respectively; (h) Distribution of lithium deposition reaction rate when charged at 1/10C, 1/4C, 1/3C and 1/2C, respectively.

overpotential as described in Eq. (8). When the overpotential of lithium plating (η_p) drops to be negative, the lithium plating is triggered. The distribution of overpotential of lithium plating along the anode thickness direction at different temperatures (−20/-25/-30 °C) is depicted in Fig. 3 (c). The x-axis denotes the dimensionless anode thickness. $\delta_- = 0$ and $\delta_- = 1$, denote the location of the interface between anode current collector and the composite anode and that between the composite anode and separator, respectively. Negative overpotential manifests the

existence of lithium plating. As the decreasing temperatures, the value of overpotential becomes more negative, which leads to the increase of the corresponding terminal voltage at the same SoC as shown in Fig. 3 (a). Moreover, the potential drop at the interface between composite anode and separator is larger than that at the other locations on anode, which implies that the lithium plating starts from the separator side. The corresponding distribution of absolute reaction rate of lithium plating along the direction of anode thickness as a function of operating temperature is plotted in Fig. 3 (d). The analysis implies that lithium deposition reaction rate increases as the decrease of temperatures. In addition, the reaction rate of lithium plating near the separator side is larger due to the relative higher lithium ion concentration, which is consistent with the analyses of overpotentials.

With the exception for the low operating temperature, high charging C-rate is another favorable factor to elicit lithium plating. The comparison of terminal voltage and corresponding estimation error at CC—CV charging with various applied current rates (1/10C-rate, 1/4C-rate, 1/3C-rate and 1/2C-rate, respectively) at the operating temperature of −20 °C between experiments and simulations is plotted in Fig. 3 (e) and (f), respectively. The simulated evolution of terminal voltage in terms of charging time has a reasonable match with the experimental one, which demonstrates the great predictive capability of electrochemical performance of LiBs by the model. To extrapolate the influence of charging C-rates, the distributions of overpotential and reaction rate of lithium plating along the anode thickness direction are presented in Fig. 3 (g) and (h), respectively. On one hand, the potential drop is enlarged as the increase of applied charging current. According to the potential governed criteria of lithium plating, no lithium deposition reaction occurs when the current of 1/10C-rate is applied to charge the cell, because the overpotential induced is positive. On the other hand, the lithium deposition reaction rate is zero when charged by 1/10C-rate current, which satisfies the conclusion that made by the analysis of overpotential evolution.

4.1.2. Mass transfer limitation (MTL)

Another criterion of lithium plating corresponds to the mass transfer of lithium ions. At low temperatures, the diffusion of lithium ions in carbon particles is slowed down, leading to the accumulation of lithium ions at the interface between carbon particles and electrolyte during charging. When the surface concentration of lithium ions in carbon particles reaches or even exceeds the maximum value that the active material of the particles can maintain, the lithium plating is prompted. Fig. 4 (a) displays the distribution of surface concentration of lithium ions across anode when charged at various C-rates (1/2C-rate, 1/3C-rate and 1/4C-rate, respectively) and operating temperatures (−20/-25/-30 °C). The maximum concentration that carbon particle can hold is plotted by a black dashed line. The surface concentration of lithium ions in solid phase increases as the ascent of charging C-rates and temperatures. Other than charging the cell by 1/2C-rate applied current at −20 °C (purple line), the surface concentration of anode particle is much smaller than the maximum value of the saturated one. Even though the gap between the surface and maximum concentration of lithium ions in anode cannot justify the existence of lithium plating, the evolution of overpotential presented in Fig. 3 gives a robust support. In order to obtain the distribution of surface concentration under the excluded charging condition more clearly, the performance in the region near the separator where the lithium plating is originated due to the oversaturated surface concentration is zoomed in. To better understand the mass transfer behaviors over the entire CC—CV charging process, the distribution of surface concentration over time at three different locations of the anode is shown in Fig. 4 (b). The variation of terminal voltage is also plotted as a reference. The increasing rate of surface concentration at each location approaches its maximum at the end of CC charging, then turns over to drop gradually at CV charging.

In summary of Figs. 3 and 4, lithium plating is prone to take place at the interface between anode and separator due to both the higher overpotential and surface concentration of lithium ions. Additionally, compared the effects of overpotential and surface concentration under various operating conditions in terms of the temporal and spatial evolutions over CC—CV charging process, charge transfer limitation is a more severe cause for lithium plating.

4.2. Analysis of lithium stripping under discharging

When discharge the LiB after charging at low temperatures, extra lithium ions coming from lithium stripping can be released on anode besides de-intercalation at the beginning. The output delivering current moving to the cathode includes that of both classical de-intercalation and lithium stripping. The extra voltage plateau represents the existence of lithium stripping and the width of the plateau is proportional to the amount of stripped lithium ions. The single cycle and multiple cycle tests are performed to validate the static and dynamic responses of the developed electrochemical model.

4.2.1. Single cycle

Fig. 5 (a) shows the discharging voltage profiles at 3 different C-rates (1/10C, 1/4C and 1/3C) immediately after charging the cell to 100% SoC at the temperature of −20 °C. The experiments and simulations are plotted by solid lines and markers, respectively. The inset provides an enlarged view of the voltage profiles at the beginning of discharging in order to observe the voltage plateaus more clearly. The simulation results can well capture the experimental measurements of

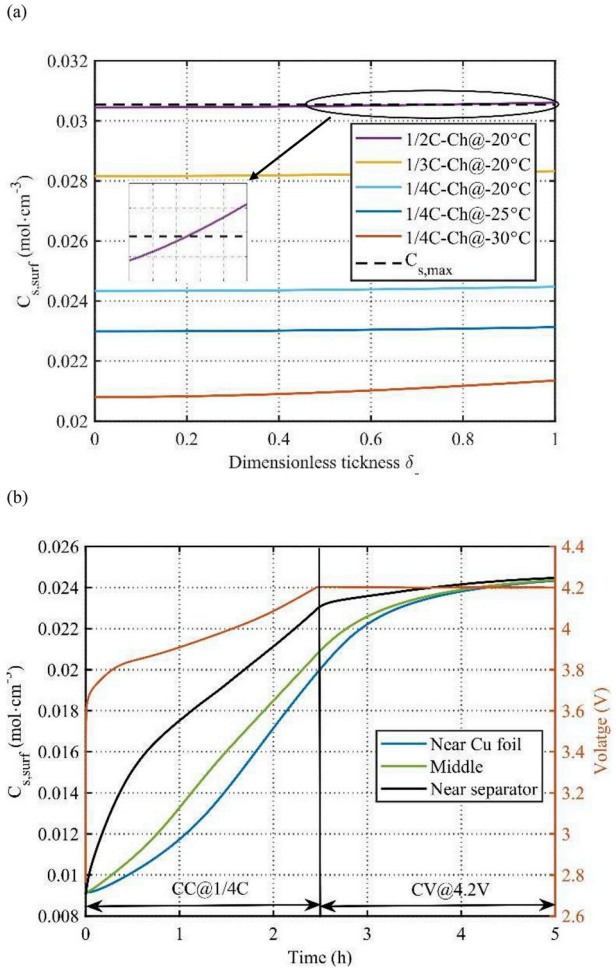

Fig. 4. (a) Distribution of surface concentration of anode particles at different temperatures and charging C-rates; (b) Distribution of surface concentration of anode particles at various locations as a function of charging time at −20 °C.

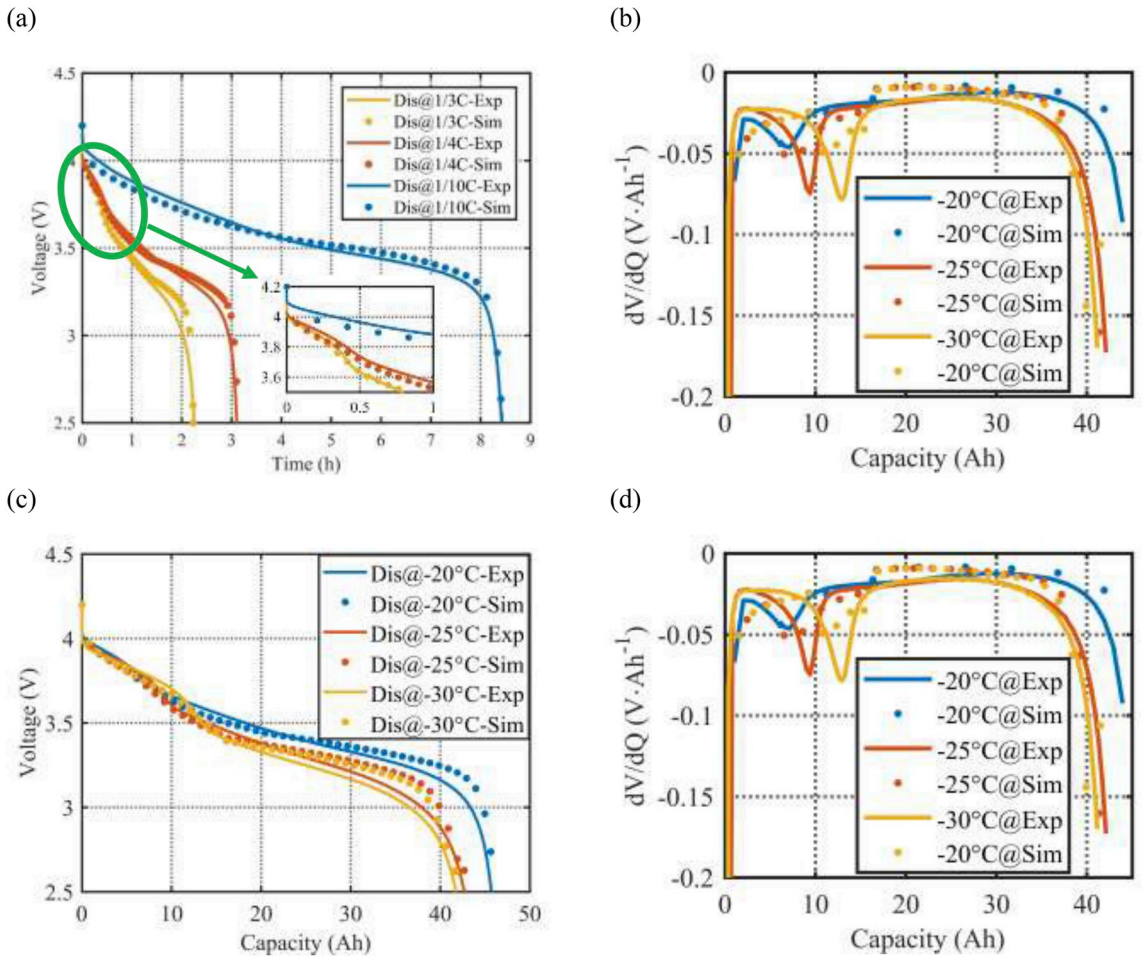

Fig. 5. (a) Comparison of discharge behaviors between experimental data and simulation results at different discharging C-rates (1/10C, 1/4C and 1/3C, respectively) at −20 °C; (b) Differential voltage analysis of the cells with different discharging C-rates applied at −20 °C; (c) Comparison of discharging voltage profiles between experiments and simulations at different temperatures; (d) Differential voltage analysis at different temperatures.

discharging voltage. In agreement with literature, the voltage plateaus can be observed at the early stage of discharging at 1/4C and 1/3C, which relate to the peaks of the differential voltage profiles (dV/dQ) in Fig. 5 (b). The characteristics of the peaks of dV/dQ is well estimated by the model with negligible discrepancies. The location where dV/dQ peak appears represents the end of lithium stripping. The discharge capacity at the dV/dQ peak equals to the total amount of the reversed capacity due to lithium stripping and the classical discharging capacity, which can be calculated by the integration of lithium stripping and main reaction rate over the electrode area and time, respectively. The reversed capacities of the cells with 1/4C and 1/3C discharging current applied are 2.18Ah and 2.72Ah, respectively. As the increase of discharging C-rates, more lithium ions can be released so that more capacity can be reversed. Fig. 5 (c) and (d) depict the comparison of discharging voltage and differential voltage analyses between experiments and simulations at different temperatures (−20/-25/-30 °C). The number of ions released by lithium stripping estimated by the developed model is proportional to the width of the extra voltage plateau at the beginning of discharging, which is approximate 2.18Ah, 3.14Ah and 4.31Ah for the cell discharged at −20 °C, −25 °C and −30 °C, respectively. The lithium stripping is accelerated as the decrease of the temperature.

4.2.2. Multiple cycle

The top subplot of Fig. 6 plots the applied current profiles in the multiple cycle tests at different temperatures. The blue and orange solid lines represent the current profiles at the temperature of −20 °C and −30 °C, respectively. The middle and bottom subplots of Fig. 6 compare the terminal voltage between experimental measurements and simulation results at −20 °C and −30 °C, respectively. Both lithium plating and lithium stripping are considered in the validation of multiple cycle tests, the modeling results have a great match with the experiments, which manifests the great capability of the model to predict the dynamic responses.

4.3. Characteristics of lithium plating/stripping over cycling

The degradation effects of LiBs after extended cycling at low temperatures are inextricably linked to the lithium plating/stripping, including loss of recyclable lithium ions, loss of AM, growth of plated lithium and secondary SEI, and the consumption of electrolyte solvents. The detailed analyses of the degradation related parameters and validation of the degradation model incorporating lithium plating/stripping are presented in section 4.3.1 and 4.3.2, respectively.

4.3.1. Analysis of degradation related parameters

To analyze the variation of the degradation related parameters inside the LiB over prolonged cycles, simulation results of lithium deposition reaction rate and other related parameters are investigated at −20 °C. The distribution of lithium deposition reaction rate along the direction of anode thickness as a function of cycle number is depicted in Fig. 7 (a). With the increase of cycle number, the lithium deposition reaction rate is accumulated at interface between carbon particles and electrolyte as the arrow indicates direction. In addition, the lithium

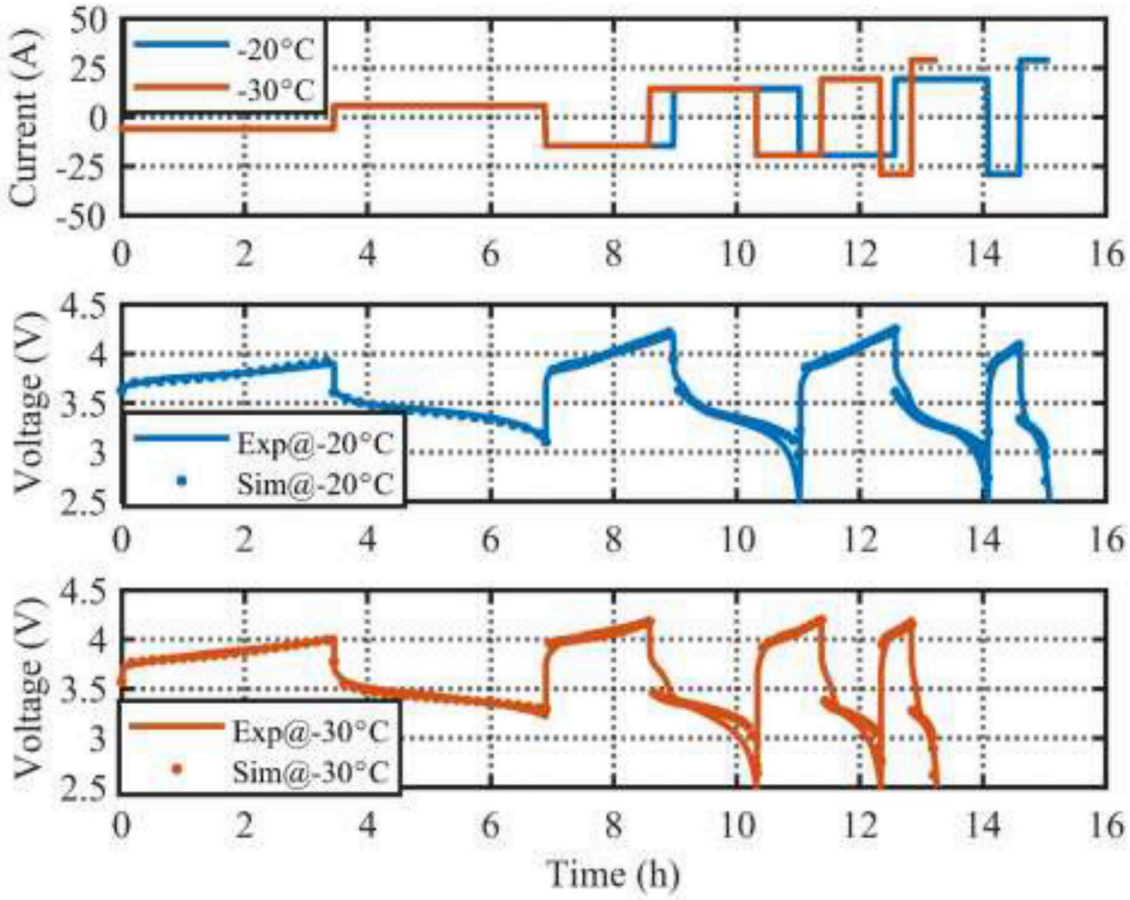

Fig. 6. Comparison of terminal voltage between experiments and simulations for multiple cycle tests at −20 °C and −30 °C.

deposition reaction rate is higher at the anode/separator interface. Correspondingly, the variations of other physical degradation parameters are plotted in Fig. 7(b–d). Due to the continuous consumption of recyclable lithium ions involved in the reaction of lithium plating, the amount of ion loss (Blue Shade), q_{total}^{Li}, is increased as the number of cycles increased. The amount of AM loss (Yellow Shade) that is induced by the reduction of the accessible area due to the growth of plated lithium and secondary SEI increases with the increasing cycle number. The total amount of ion loss and AM loss is compared with the actual capacity fade (Green Shade) measured by the experiments, which shows a great match in Fig. 7 (b). The variations of resistance of plated lithium ($R_{plating}$) and electrode volume fraction (ε_s) in terms of cycle number across the anode are plotted in Fig. 7 (c). As the reactants of the chemical reaction described in Eqs. (17) and (18), electrolyte solvents are consumed continuously, which leads to the decrease of electrolyte volume fraction (ε_e), as shown in the upper subplot of Fig. 7 (d). The lower subplot shows the increase of resistance of deposit layer (DL) that is defined as a layer located at anode/separator interface. The analyses of the degradation effects of lithium plating based on the variation of the electrochemical parameters can be summarized in Table 5.

4.3.2. Model validation of end-of-life (EoL)

According to the analyses of overpotential and concentration in terms of temporal and spatial distribution, both the temperatures and charging C-rates have profound impacts on the lithium plating, while the temperatures and discharging C-rates have influences on the lithium stripping. To explore the effects on the prolonged cycles, both lithium plating and lithium stripping are considered. The comparison of discharge terminal voltage with 1/3C-rate discharge current applied between simulation results obtained by the physics-based degradation model and experimental measurements at different operating conditions are plotted in Fig. 8(a–d), while those for the cells performed multiple cycling tests are plotted in Fig. 8(e and f). The solid lines and markers represent the experiments and simulations, respectively. The influences of charging C-rates on the long-term cycling tests are discussed between subplot (a) and (b), while those of temperatures are summarized in subplot (c) and (d). In Fig. 8 (d), the terminal voltage is overestimated at the 6th cycle whose capacity fade is about 43.9%. Usually, the EV battery is considered as EoL when its capacity drops below 80% of its nominal capacity, or 70% at the worst case. When the battery continues to get further aged, not only lithium plating/stripping from the aspect of electrochemistry, but also mechanical failure needs to be considered. In this paper, the neglect of the mechanical failure makes the model not be capable of predicting the electrochemical performance when the capacity fade of the cell reaches 43.9%.

Capacity fade is one of the most significant criteria to evaluate performance of degraded LiBs. The comparisons of simulated capacity and the Ah-based measured capacity as the function of cycle number at various charging C-rates and temperatures are shown in the upper subplot of Fig. 8 (g). The markers, circles and crosses, denote the measurements and simulations, respectively. Furthermore, the corresponding error between measurements and simulation results is plotted in the lower subplot. In order to display the capacity variations comparably, the SOH in terms of capacity and its corresponding estimation error are calculated in Eq. (21) and Eq. (22), respectively.

$$\mathrm{SOH}_Q = \frac{Q_{aged,cell}}{Q_{fresh,cell}} \tag{21}$$

$$Q_{error} = \frac{Q_{\exp} - Q_{sim}}{Q_{\exp}} \times 100\% \tag{22}$$

Apart from a relatively large deviation of the last capacity

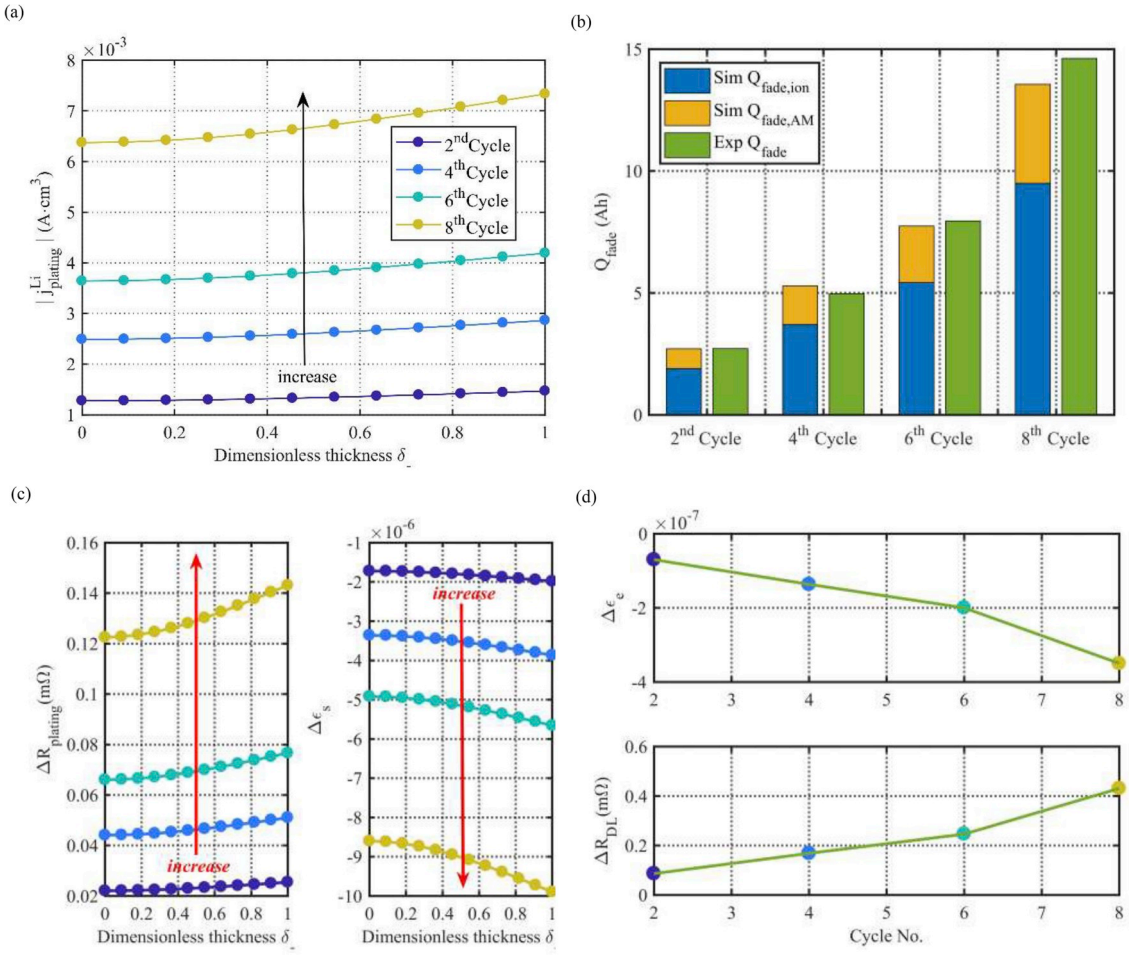

Fig. 7. Analysis of degradation parameters in the lithium deposition reaction. (a) Lithium deposition reaction rate; (b) Ion & AM loss; (c) Variation of resistance of plated lithium and volume fraction of anode; (d) Variation of volume fraction of electrolyte and resistance of DL.

estimation at −30 °C, other deviation of simulations over experiments is less than 3%. With regard to the comparisons of capacity for multiple cycling tests, the error of capacity estimation is within 1.5% when the capacity fade is less than 30%.

5. Conclusion

A physics-based electrochemical-thermal model considering degradation effects of lithium plating/stripping is developed to investigate the electrochemical performances of LiBs at subzero temperatures. The model is validated against both the fresh and aged NMC/Carbon cells through a series of experiments at different operating conditions, including temperatures, charging and discharging current rates. The model has a reasonable match with the experimental results, whose estimation error is less than 4%. Modeling analyses of lithium plating are performed in the aspects of charge and mass transfer processes. Negative overpotential or oversaturated surface concentration of lithium ions denote the existence of lithium plating. The model also well captures the characteristics of the extra voltage plateau which represents the existence of lithium stripping at discharging. Differential voltage analyses are used to characterize the amount of reversed capacity by the integration of reaction rate of lithium stripping over time and electrode area. It is illustrated that the amount of reversed capacity increases as the increase of discharging C-rates. Furthermore, the model quantitatively manifests the degradation effects, including loss of lithium inventory, loss of anode active material, growth of plated lithium and secondary SEI and consumption of electrolyte solvents. Both single and multiple cycling tests are preformed to validate the static and dynamic responses of the model, which match reasonably with experimental measurements with respect to the terminal voltage and capacity retention. Except for the capacity drops below 70% of its nominal capacity, the error of the capacity estimation remains within 3%.

In the future work, the model needs to be improved to facilitate the in-depth investigations on the side reaction and lithium plating/

Table 5
Degradation effects and parameters of lithium deposition reaction.

Causes	Effects	Degradation parameters	Consequences
Lithium deposition reaction rate $\left\|j^{Li}_{plating}\right\|\uparrow$	Ion loss	$q^{Li}_{total}(t)\uparrow$	Capacity fade
	AM loss	Electrode volume fraction $\varepsilon_s\downarrow$	Capacity fade
	Plated Li growth	Resistance of plated lithium $R_{plating}\uparrow$	Impedance rise
	DL growth	Resistance of DL $R_{DL}\uparrow$	Impedance rise
	Electrolyte consumption	Electrolyte volume fraction $\varepsilon_e\downarrow$	Impedance rise

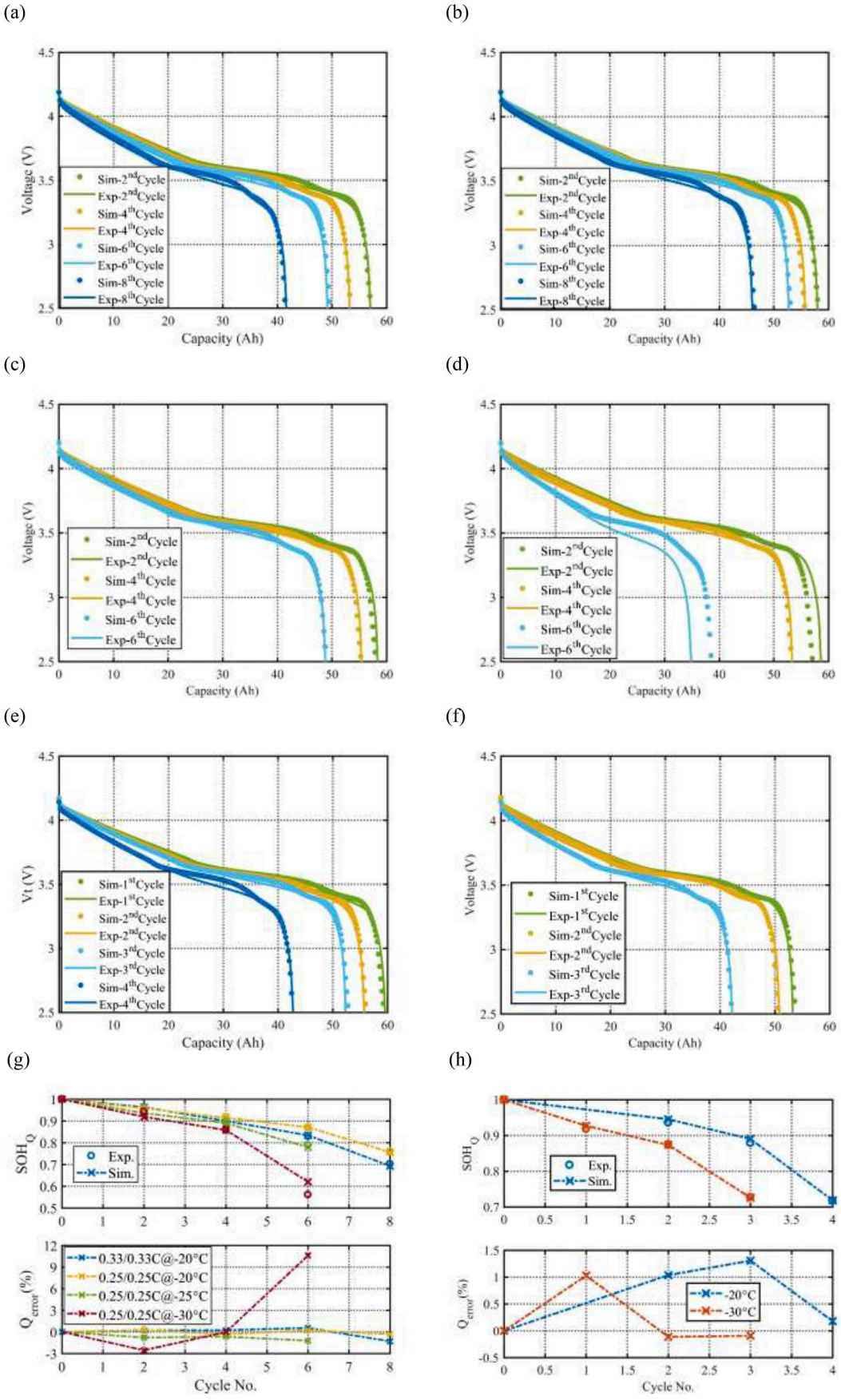

(caption on next page)

Fig. 8. Comparison of discharge behaviors by 1/3C-rate current at various cycling conditions. (a) Cycling by 1/3C-rate charging and discharging current at −20 °C; (b) Cycling by 1/4C-rate charging and discharging current at −20 °C; (c) Cycling by 1/4C-rate charging and discharging current at −25 °C; (d) Cycling by 1/3C-rate charging and discharging current at −30 °C; (e) Multiple cycling by pulse currents at −20 °C; (f) Multiple cycling by pulse currents at −30 °C; (g) Comparison between Ah-based measured capacity and simulated capacity at various charging C-rates (1/3C-rate, 1/4C-rate) and temperatures (−20/-25/-30 °C); (h) Comparison between Ah-based measured capacity and simulated capacity at multiple cycling tests at −20 °C and −30 °C.

stripping at the same time. Moreover, other degradation effects, such as mechanical failure and cathode degradation need to be considered for the deep cycling of the LiBs.

References

[1] Z. Li, J. Huang, B. Yann Liaw, V. Metzler, J. Zhang, A review of lithium deposition in lithium-ion and lithium metal secondary batteries, J. Power Sources 254 (2014) 168–182, https://doi.org/10.1016/j.jpowsour.2013.12.099.

[2] H.J. Ploehn, P. Ramadass, R.E. White, Solvent diffusion model for aging of lithium-ion battery cells, J. Electrochem. Soc. 151 (2004) A456, https://doi.org/10.1149/1.1644601.

[3] S. Santhanagopalan, Q. Zhang, K. Kumaresan, R.E. White, Parameter estimation and life modeling of lithium-ion cells, J. Electrochem. Soc. 155 (2008) A345–A353, https://doi.org/10.1149/1.2839630.

[4] Q. Zhang, R.E. White, Capacity fade analysis of a lithium ion cell, J. Power Sources 179 (2008) 793–798, https://doi.org/10.1016/j.jpowsour.2008.01.028.

[5] Y. Zhang, C.Y. Wang, X. Tang, Cycling degradation of an automotive $LiFePO_4$ lithium-ion battery, J. Power Sources 196 (2011) 1513–1520, https://doi.org/10.1016/j.jpowsour.2010.08.070.

[6] J. Vetter, P. Novák, M.R. Wagner, C. Veit, K.C. Möller, J.O. Besenhard, M. Winter, M. Wohlfahrt-Mehrens, C. Vogler, A. Hammouche, Ageing mechanisms in lithium-ion batteries, J. Power Sources 147 (2005) 269–281, https://doi.org/10.1016/j.jpowsour.2005.01.006.

[7] A. Barré, B. Deguilhem, S. Grolleau, M. Gérard, F. Suard, D. Riu, A review on lithium-ion battery ageing mechanisms and estimations for automotive applications, J. Power Sources 241 (2013) 680–689, https://doi.org/10.1016/j.jpowsour.2013.05.040 Review.

[8] D. Anseán, M. Dubarry, A. Devie, B.Y. Liaw, V.M. García, J.C. Viera, M. González, Operando lithium plating quantification and early detection of a commercial $LiFePO_4$ cell cycled under dynamic driving schedule, J. Power Sources 356 (2017) 36–46, https://doi.org/10.1016/j.jpowsour.2017.04.072.

[9] J.C. Burns, D.A. Stevens, J.R. Dahn, In-situ detection of lithium plating using high precision coulometry, J. Electrochem. Soc. 162 (2015) A959–A964, https://doi.org/10.1149/2.0621506jes.

[10] M. Petzl, M.A. Danzer, Nondestructive detection, characterization, and quantification of lithium plating in commercial lithium-ion batteries, J. Power Sources 254 (2014) 80–87, https://doi.org/10.1016/j.jpowsour.2013.12.060.

[11] S. Tippmann, D. Walper, L. Balboa, B. Spier, W.G. Bessler, Low-temperature charging of lithium-ion cells part I: electrochemical modeling and experimental investigation of degradation behavior, J. Power Sources 252 (2014) 305–316, https://doi.org/10.1016/j.jpowsour.2013.12.022.

[12] Y. Ji, Y. Zhang, C.-Y. Wang, Li-Ion cell operation at low temperatures, J. Electrochem. Soc. 160 (2013) A636–A649, https://doi.org/10.1149/2.047304jes.

[13] M. Petzl, M. Kasper, M.A. Danzer, Lithium plating in a commercial lithium-ion battery - a low-temperature aging study, J. Power Sources 275 (2015) 799–807, https://doi.org/10.1016/j.jpowsour.2014.11.065.

[14] A. Senyshyn, M.J. Mühlbauer, O. Dolotko, H. Ehrenberg, Low-temperature performance of Li-ion batteries: the behavior of lithiated graphite, J. Power Sources 282 (2015) 235–240, https://doi.org/10.1016/j.jpowsour.2015.02.008.

[15] V. Zinth, C. Von Lüders, M. Hofmann, J. Hattendorff, I. Buchberger, S. Erhard, J. Rebelo-Kornmeier, A. Jossen, R. Gilles, Lithium plating in lithium-ion batteries at sub-ambient temperatures investigated by in situ neutron diffraction, J. Power Sources 271 (2014) 152–159, https://doi.org/10.1016/j.jpowsour.2014.07.168.

[16] T. Waldmann, A. Iturrondobeitia, M. Kasper, N. Ghanbari, F. Aguesse, E. Bekaert, L. Daniel, S. Genies, I.J. Gordon, M.W. Löble, E. De Vito, M. Wohlfahrt-Mehrens, Review—post-mortem analysis of aged lithium-ion batteries: disassembly methodology and physico-chemical analysis techniques, J. Electrochem. Soc. 163 (2016) 2149–2164, https://doi.org/10.1149/2.1211609jes.

[17] S. Schindler, M. Bauer, M. Petzl, M.A. Danzer, Voltage relaxation and impedance spectroscopy as in-operando methods for the detection of lithium plating on graphitic anodes in commercial lithium-ion cells, J. Power Sources 304 (2016) 170–180, https://doi.org/10.1016/j.jpowsour.2015.11.044.

[18] M. Ouyang, Z. Chu, L. Lu, J. Li, X. Han, X. Feng, G. Liu, Low temperature aging mechanism identification and lithium deposition in a large format lithium iron phosphate battery for different charge profiles, J. Power Sources 286 (2015) 309–320, https://doi.org/10.1016/j.jpowsour.2015.03.178.

[19] C. Uhlmann, J. Illig, M. Ender, R. Schuster, E. Ivers-Tiffée, In situ detection of lithium metal plating on graphite in experimental cells, J. Power Sources 279 (2015) 428–438, https://doi.org/10.1016/j.jpowsour.2015.01.046.

[20] B. Stiaszny, J.C. Ziegler, E.E. Krauß, J.P. Schmidt, E. Ivers-Tiffée, Electrochemical characterization and post-mortem analysis of aged $LiMn_2O_4$-$Li(Ni_{0.5}Mn_{0.3}Co_{0.2})O_2$/graphite lithium ion batteries. Part I: cycle aging, J. Power Sources 251 (2014) 439–450, https://doi.org/10.1016/j.jpowsour.2013.11.080.

[21] B. Zhao, Y. Jiang, H. Zhang, H. Tao, M. Zhong, Z. Jiao, Morphology and electrical properties of carbon coated $LiFePO_4$ cathode materials, J. Power Sources 189 (2009) 462–466, https://doi.org/10.1016/j.jpowsour.2008.12.069.

[22] M. Klett, R. Eriksson, J. Groot, P. Svens, K. Ciosek Högström, R.W. Lindström, H. Berg, T. Gustafson, G. Lindbergh, K. Edström, Non-uniform aging of cycled commercial LiFePO4/graphite cylindrical cells revealed by post-mortem analysis, J. Power Sources 257 (2014) 126–137, https://doi.org/10.1016/j.jpowsour.2014.01.105.

[23] T. Waldmann, M. Wilka, M. Kasper, M. Fleischhammer, M. Wohlfahrt-Mehrens, Temperature dependent ageing mechanisms in Lithium-ion batteries - a post-mortem study, J. Power Sources 262 (2014) 129–135, https://doi.org/10.1016/j.jpowsour.2014.03.112.

[24] S.J. An, J. Li, Y. Sheng, C. Daniel, D.L. Wood Iii, Long-Term Lithium-ion battery performance improvement via ultraviolet light treatment of the graphite anode, J. Electrochem. Soc. 163 (2016) 2866–2875, https://doi.org/10.1149/2.0171614jes.

[25] W. Lu, C.M. López, N. Liu, J.T. Vaughey, A. Jansen, D.W. Dees, Overcharge effect on morphology and structure of carbon electrodes for lithium-ion batteries, J. Electrochem. Soc. 159 (2012) A566, https://doi.org/10.1149/2.jes035205.

[26] N. Liao, B. Zheng, M. Zhang, W. Xue, Atomic investigation on reversible lithium storage in amorphous silicon oxycarbide as a high power anode material, J. Mater. Chem. A. 4 (2016) 12328–12333, https://doi.org/10.1039/c6ta04729g.

[27] P. Arora, Mathematical modeling of the lithium deposition overcharge reaction in lithium-ion batteries using carbon-based negative electrodes, J. Electrochem. Soc. 146 (1999) 3543, https://doi.org/10.1149/1.1392512.

[28] M. Doyle, T.F. Fuller, J. Newmann, Modeling of galvanostatic charge and discharge of the Lithium/Polymer/Insertion cell, J. Electrochem. Soc. 140 (1993) 1526–1532, https://doi.org/10.1149/1.2221597.

[29] M. Tang, P. Albertus, J. Newman, Two-dimensional modeling of lithium deposition during cell charging, J. Electrochem. Soc. 156 (2009) A390, https://doi.org/10.1149/1.3095513.

[30] R.D. Perkins, A.V. Randall, X. Zhang, G.L. Plett, Controls oriented reduced order modeling of lithium deposition on overcharge, J. Power Sources 209 (2012) 318–325, https://doi.org/10.1016/j.jpowsour.2012.03.003.

[31] H. Ge, T. Aoki, N. Ikeda, S. Suga, T. Isobe, Z. Li, Y. Tabuchi, J. Zhang, Investigating lithium plating in lithium-ion batteries at low temperatures using electrochemical model with NMR assisted parameterization, J. Electrochem. Soc. 164 (2017) A1050–A1060, https://doi.org/10.1149/2.0461706jes.

[32] X.G. Yang, Y. Leng, G. Zhang, S. Ge, C.Y. Wang, Modeling of lithium plating induced aging of lithium-ion batteries: transition from linear to nonlinear aging, J. Power Sources 360 (2017) 28–40, https://doi.org/10.1016/j.jpowsour.2017.05.110.

[33] X. Zhao, Y. Bi, S.-Y. Choe, Development and validation of a reduced order model incorporating a semi-empirical degradation model for pouch type $LiFePO_4$/graphite cells, SAE Int. J. Altern. Powertrains. 6 (2017), https://doi.org/10.4271/2017-01-1218 2017-01-1218.

[34] X. Zhao, Y. Bi, S.-Y. Choe, S.-Y. Kim, An integrated reduced order model considering degradation effects for $LiFePO_4$/graphite cells, Electrochim. Acta 280 (2018) 41–54, https://doi.org/10.1016/J.ELECTACTA.2018.05.091.